

Prediction and observation of the first antiferromagnetic topological insulator

M. M. Otrokov,^{1,2,3,*} I. I. Klimovskikh,³ H. Bentmann,⁴ A. Zeugner,⁵ Z. S. Aliev,^{6,7} S. Gass,⁸
 A. U. B. Wolter,⁸ A. V. Koroleva,³ D. Estyunin,³ A. M. Shikin,³ M. Blanco-Rey,^{9,10} M. Hoffmann,¹¹
 A. Yu. Vyazovskaya,^{2,3} S. V. Ereemeev,^{12,2} Yu. M. Koroteev,^{12,2} I. R. Amiraslanov,⁶ M. B. Babanly,¹³
 N. T. Mamedov,⁶ N. A. Abdullayev,⁶ V. N. Zverev,¹⁴ B. Büchner,^{8,15} E. F. Schwier,¹⁶ S. Kumar,¹⁶ A. Kimura,¹⁷
 L. Petaccia,¹⁸ G. Di Santo,¹⁸ R. C. Vidal,⁴ S. Schatz,⁴ K. Kißner,⁴ C. H. Min,⁴ Simon K. Moser,¹⁹
 T. R. F. Peixoto,⁴ F. Reinert,⁴ A. Ernst,^{11,20} P. M. Echenique,^{1,9,10} A. Isaeva,⁵ and E. V. Chulkov^{10,9,3,1}

¹*Centro de Física de Materiales (CFM-MPC), Centro Mixto CSIC-UPV/EHU,
 20018 Donostia-San Sebastián, Basque Country, Spain*

²*Tomsk State University, 634050 Tomsk, Russia*

³*Saint Petersburg State University, 198504 Saint Petersburg, Russia*

⁴*Experimentelle Physik VII, Universität Würzburg, Am Hubland, D-97074 Würzburg, Germany*

⁵*Technische Universität Dresden, Faculty of Chemistry and Food Chemistry, Helmholtzstrasse 10, 01069 Dresden, Germany*

⁶*Institute of Physics, Azerbaijan National Academy of Sciences, 1143 Baku, Azerbaijan*

⁷*Azerbaijan State Oil and Industry University, AZ1010 Baku, Azerbaijan*

⁸*Leibniz-Institut für Festkörper- und Werkstoffforschung Dresden e. V.,
 Institut für Festkörperforschung, D-01069 Dresden, Germany*

⁹*Departamento de Física de Materiales UPV/EHU,
 20080 Donostia-San Sebastián, Basque Country, Spain*

¹⁰*Donostia International Physics Center (DIPC),
 20018 Donostia-San Sebastián, Basque Country, Spain*

¹¹*Institut für Theoretische Physik, Johannes Kepler Universität, A 4040 Linz, Austria*

¹²*Institute of Strength Physics and Materials Science,
 Russian Academy of Sciences, 634021 Tomsk, Russia*

¹³*Institute of Catalysis and Inorganic Chemistry,
 Azerbaijan National Academy of Science, AZ1143 Baku, Azerbaijan*

¹⁴*Institute of Solid State Physics, Russian Academy of Sciences, Chernogolovka 142432, Russia*

¹⁵*Institut für Festkörper- und Materialphysik, Technische Universität Dresden, D-01062 Dresden, Germany*

¹⁶*Hiroshima Synchrotron Radiation Center, Hiroshima University, Higashi-Hiroshima, Hiroshima 739-0046, Japan*

¹⁷*Department of Physical Sciences, Graduate School of Science,
 Hiroshima University, Higashi-Hiroshima, Hiroshima 739-8526, Japan*

¹⁸*Elettra Sincrotrone Trieste, Strada Statale 14 km 163.5, 34149 Trieste, Italy*

¹⁹*Advanced Light Source, Lawrence Berkeley National Laboratory, Berkeley, CA 94720, USA*

²⁰*Max-Planck-Institut für Mikrostrukturphysik, Weinberg 2, D-06120 Halle, Germany*

(Dated: March 10, 2024)

Despite immense advances in the field of topological materials, the antiferromagnetic topological insulator (AFMTI) state, predicted in 2010, has been resisting experimental observation up to now. Here, using density functional theory and Monte Carlo method we predict and by means of structural, transport, magnetic, and angle-resolved photoemission spectroscopy measurements confirm for the first time realization of the AFMTI phase, that is hosted by the van der Waals layered compound MnBi_2Te_4 . An interlayer AFM ordering makes MnBi_2Te_4 invariant with respect to the combination of the time-reversal (Θ) and primitive-lattice translation ($T_{1/2}$) symmetries, $S = \Theta T_{1/2}$, which gives rise to the Z_2 topological classification of AFM insulators, Z_2 being equal to 1 for this material. The S -breaking (0001) surface of MnBi_2Te_4 features a giant bandgap in the topological surface state thus representing an ideal platform for the observation of such long-sought phenomena as the quantized magnetoelectric coupling and intrinsic axion insulator state.

I. INTRODUCTION

A number of remarkable experimental observations and theoretical predictions recently made for antiferromagnetic (AFM) materials indicate clearly that they can be of great practical importance^{1–9}. Indeed, such effects as magnetoresistance, spin torque, and ultrafast dynamics observed in certain AFM materials promise significant advances in novel electronics³. At the crossroad of antiferromagnetism and the emerging field of “topotronics”, i.e. electronics based on the properties of topologically-

nontrivial systems^{10–12}, an AFM topological insulator (AFMTI) emerges¹³, predicted to give rise to both exotic physics¹⁴ and practically relevant phenomena^{14,15}. An AFMTI can be realized in materials breaking both time-reversal Θ and primitive-lattice translational symmetry $T_{1/2}$, but preserving their combination $S = \Theta T_{1/2}$, that leads to a Z_2 topological classification¹³. To date, no AFMTI was found.

Here, using state-of-the-art *ab initio* techniques and Monte Carlo simulations along with the structural, transport, magnetic, and photoemission measurements we dis-

cover a first ever AFMTI compound, MnBi_2Te_4 . Built of septuple layer blocks stacked along the $[0001]$ direction and weakly bound to each other by van der Waals forces, MnBi_2Te_4 develops an interlayer AFM state, in which ferromagnetic (FM) Mn layers of neighboring blocks are coupled antiparallel to each other, while the easy axis of the staggered magnetization points perpendicular to the blocks. This type of magnetic structure makes MnBi_2Te_4 S -symmetric in bulk, while the strong spin-orbit coupling (SOC) of Bi and Te leads to the appearance of an inverted bandgap of about 200 meV, converting the material in a three-dimensional (3D) AFMTI. Unlike the bulk, the (0001) surface of MnBi_2Te_4 , i.e. its natural cleavage plane, is S -breaking¹³, which causes the opening of a giant gap in the Dirac point (DP), as evidenced by our photoemission measurements. These results promise to facilitate the eventual observations of such exotic phenomena as quantized magnetoelectric coupling^{13,16–18} and the axion insulator state^{14,19–21}, both being intimately related to the AFMTI state of matter.

II. THEORETICAL PREDICTION

The $R\bar{3}m$ -group structure of bulk MnBi_2Te_4 (Fig. 1a) was reported in Ref. [22]. Since the magnetism of MnBi_2Te_4 was not experimentally investigated, we begin our study by calculating the exchange coupling parameters J from first principles. It is seen in Figs. 1b and 1c that among the intralayer interactions J^\parallel the one between first nearest neighbors in the Mn layer is clearly dominant ($J_{0,1}^\parallel \simeq 0.09 \text{ meV}/\mu_B^2$), while the interactions with more distant neighbors are an order of magnitude weaker. The calculated single-site spin stiffness coefficient ($J_0^\parallel = \sum_{j \neq 0} J_{0,j}^\parallel$; the sum runs over *all* $(0,j)$ -pairs of interacting moments), that accounts for the energy required to flip a local magnetic moment, is positive and equal to $0.4 \text{ meV}/\mu_B^2$ for the intralayer coupling. Therefore, an FM ordering is expected within each septuple layer (SL) block of MnBi_2Te_4 . In contrast, the *interlayer* coupling constants J^\perp are mostly negative. The corresponding single-site spin stiffness coefficient J_0^\perp is also negative and equal to $-0.022 \text{ meV}/\mu_B^2$, which means that the overall coupling between neighboring Mn layers is antiferromagnetic. This conclusion is consistent with the results of previous total-energy calculations²³, confirming that the interlayer AFM structure, shown in Fig. 1d, is the magnetic ground state of MnBi_2Te_4 . We then calculate the magnetic anisotropy energy of MnBi_2Te_4 that turns out to be positive and equal to 0.225 meV per Mn atom, indicating the easy axis with an out-of-plane orientation of the local magnetic moments ($\pm 4.607\mu_B$). Our Monte Carlo simulations confirm the interlayer AFM structure suggested by *ab initio* calculations with a Néel temperature (T_N) of 3D ordering of 25.4 K (Supplementary Figure 1).

Given the magnetic ground state, the bulk electronic structure was calculated. As shown in Fig. 1e, the sys-

tem is insulating, the fundamental bandgap value, determined from the GGA+ U calculation of the density of states (DOS), being equal to 225 meV. The gap magnitude decreases just slightly (to 220 meV) if the HSE06 functional is used, which is known to provide accurate semiconductor gaps and a better description of correlations. To determine whether the gap is negative (inverted), we performed the DOS calculations decreasing the SOC constant λ stepwise from its natural value λ_0 to $\lambda = 0.5\lambda_0$. It was found that at $\lambda/\lambda_0 \simeq 0.675$ the gap is closed, while at other λ/λ_0 ratios it is nonzero, which points towards a nontrivial topology of MnBi_2Te_4 .

Mong, Essin, and Moore¹³ introduced a Z_2 classification of AFMTIs, that is provided by a combination $S = \Theta T_{1/2}$ of the time-reversal Θ and primitive-lattice translational symmetry $T_{1/2}$. Since MnBi_2Te_4 is S -symmetric, the Z_2 invariant can be calculated based on the occupied bands parities^{13,24}. We find $Z_2 = 1$, which unambiguously classifies MnBi_2Te_4 as AFMTI. Note that, unlike GdBiPt , which was predicted^{13,25,26} (but still not experimentally confirmed) to be an AFMTI under pressure, MnBi_2Te_4 is an intrinsic AFMTI.

The implication of the bulk bandgap inversion in a TI is seen at its surface, where the topological phase transition is manifested by the appearance of the topological surface state. In the case of nonmagnetic TIs, this surface state is gapless^{10–12}, but at the (0001) surface of the AFMTI MnBi_2Te_4 we find, however, a 88-meV-wide bandgap (Fig. 1f). Indeed, unlike conventional strong nonmagnetic TIs^{10–12}, not all of the AFMTI surfaces are gapless, but typically only those preserving the $S = \Theta T_{1/2}$ symmetry¹³. In the case of an FM layer near the AFMTI surface, this symmetry is broken and an out-of-plane magnetization component opens a surface gap¹³.

III. EXPERIMENTAL CONFIRMATION

For the first time, high-quality MnBi_2Te_4 single crystals were grown at the TU Dresden (hereinafter D samples, Fig. 2a) and at IP Baku (B samples, Fig. 2b) as described in the Methods section. X-ray single-crystal diffraction experiments confirm the lattice symmetry (space group $R\bar{3}m$) found in Ref. [22]. The structure refinement yields some degree of statistical cation disorder in the Mn and Bi positions (Fig. 2c) in contrast to earlier reported ordered model²². Mn/Bi antisite defects in two fully occupied cation positions do not, however, lead to a change of translational symmetry or superstructure ordering. Energy-dispersive X-ray spectroscopy reproducibly results in the stoichiometric MnBi_2Te_4 composition, ruling out a possibility of large compositional variations in our samples. Similar cation intermixing was observed in the GeBi_2Te_4 TI compound^{27,28} and other mixed $X\text{Bi}_2\text{Te}_4$ ($X = \text{Sn}, \text{Pb}$) semiconductors isostructural to MnBi_2Te_4 , and is, therefore, characteristic for these materials.

Temperature- and field-dependent magnetization mea-

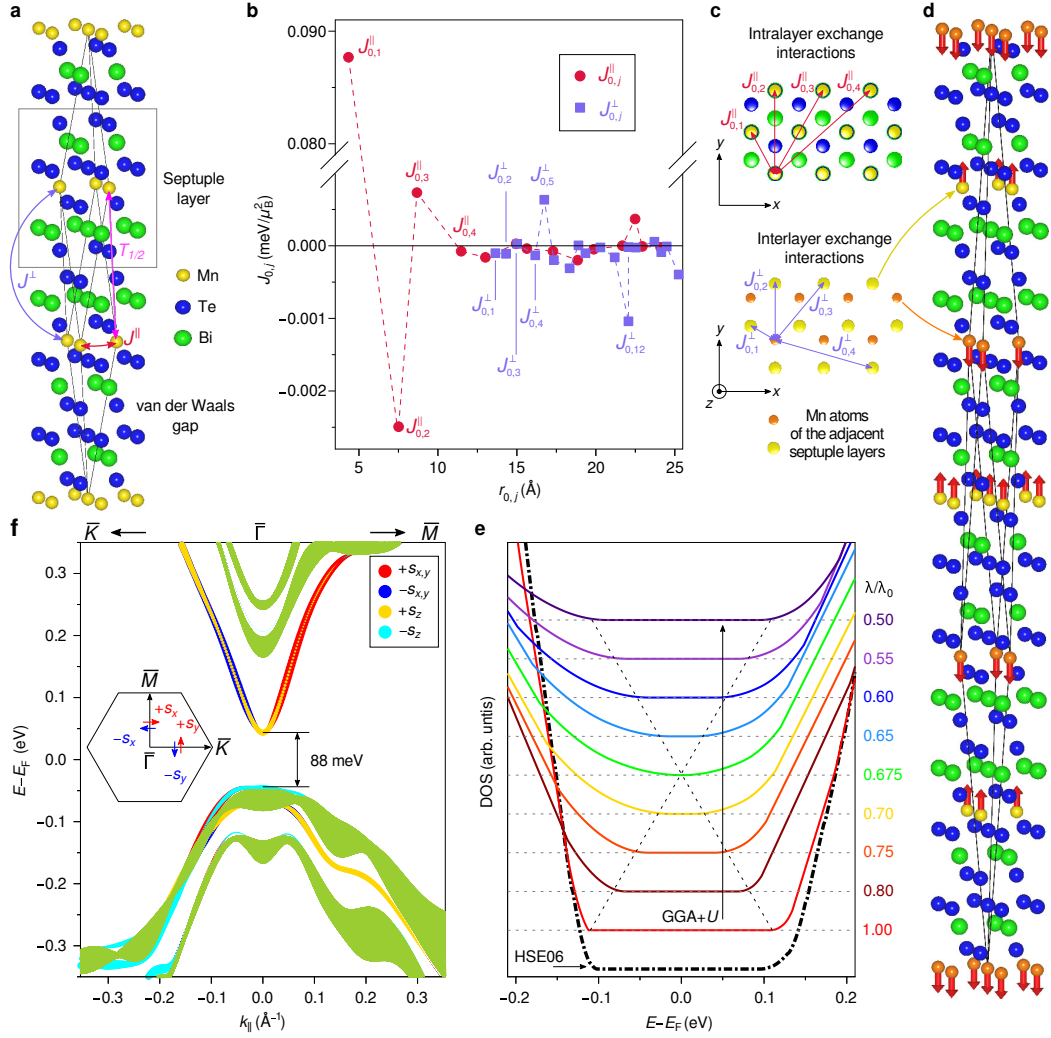


Figure 1. **a**, Atomic structure of the $R\bar{3}m$ bulk MnBi_2Te_4 with yellow, blue and green balls showing Mn, Te and Bi atoms, respectively. The "nonmagnetic" rhombohedral primitive unit cell is shown by gray lines; the $T_{1/2}$ translation is shown in magenta. **b**, Calculated exchange constants $J_{0,j}$ (in meV/μ_B^2) for the intralayer (J^{\parallel} , red circles) and interlayer (J^{\perp} , blue squares) pair interactions as a function of the Mn-Mn distance, $r_{0,j}$. **c**, Schematic topview representation of magnetic interactions in the Mn layer (upper part) and between two neighboring Mn layers (lower part). **d**, Magnetic unit cell corresponding to the interlayer AFM state. **e**, Total DOS of bulk MnBi_2Te_4 calculated for the interlayer AFM state shown in **d**, using the HSE06 exchange-correlation functional (dash-point black line) and GGA+ U approach (solid color lines). In the latter case, the evolution of the DOS with the change of the SOC constant λ is shown. **f**, Spin-resolved electronic structure of the $\text{MnBi}_2\text{Te}_4(0001)$ surface. The size of color circles reflects the value and sign of the spin vector cartesian projections, with red/blue colors corresponding to the positive/negative s_x and s_y components (perpendicular to k_{\parallel}), and gold/cyan to the out-of-plane components $+s_z/-s_z$. The green areas correspond to the bulk bandstructure projected onto the surface Brillouin zone.

measurements performed on D samples (Fig. 2d,e) establish a 3D AFM order below $T_N = 24.2(5)$ K, in agreement with the prediction by the Monte Carlo method. Below T_N , a strongly anisotropic magnetic susceptibility χ is observed, that decreases much steeper for $H \perp (0001)$ plane. No splitting between zero-field-cooled and field-cooled-warming curves was observed. The paramagnetic regime above T_N was fitted with a modified Curie-Weiss law, $\chi(T) = \chi_0 + C/(T - \Theta_{CW})$, in the 100 K to 250 K range. Here, χ_0 stands for a temperature-independent magnetic susceptibility of both diamagnetic closed elec-

tron shells and a Pauli paramagnetic contribution due to some degree of metallicity in this material (see below). $C/(T - \Theta_{CW})$ considers a temperature-dependent Curie-Weiss susceptibility of mostly localized Mn moments. The fitted effective paramagnetic moment of $5.0(2)\mu_B$ is in rough agreement with the high-spin configuration of Mn^{2+} ($S = 5/2$), while the small and positive value of the Curie-Weiss temperature ($\Theta_{CW} = 3(3)$ K) strongly depends on the fitted χ_0 contribution. However, given the AFM order below $T_N = 24.2(5)$ K, it indicates competing AFM and FM exchange couplings in MnBi_2Te_4 .

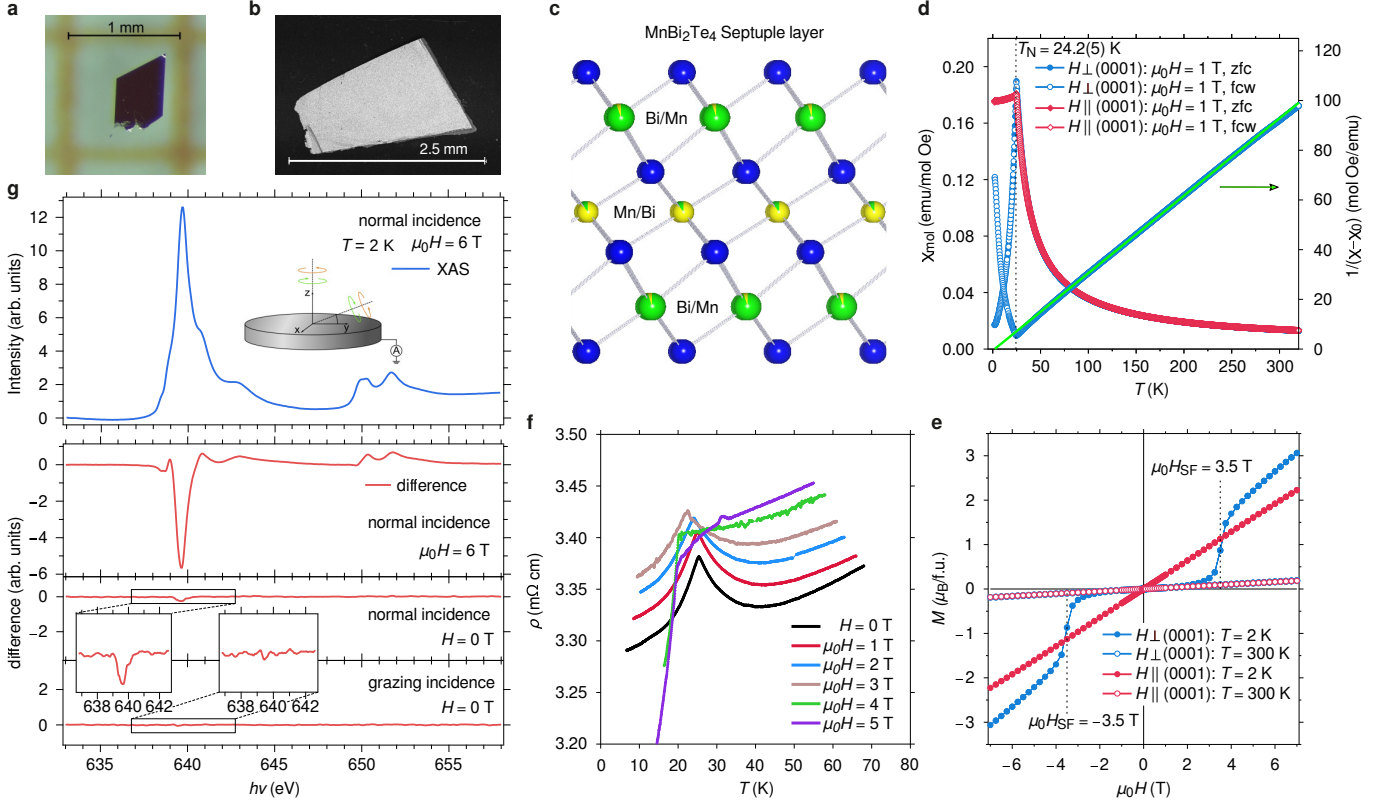


Figure 2. **a, b**, MnBi₂Te₄ single crystals: D sample (**a**, optical microscope image) and B sample (**b**, scanning electron microscope image). **c**, A schematic illustration of the MnBi₂Te₄ single SL with antisite Mn/Bi defects in fully occupied cationic sites. **d**, Magnetic susceptibility (left axis of ordinates) of phase-pure MnBi₂Te₄ as a function of temperature measured in an external magnetic field of $\mu_0 H = 1$ T in zero-field-cooled (zfc) and field-cooled-warming (fcw) conditions along with the temperature-dependent reciprocal susceptibility (right axis of ordinates) for $H \perp (0001)$ plane. The green line is a modified Curie-Weiss fit to the high-temperature data ($\chi_0 = 0.0028(3)$ emu/mol Oe); for details see text. **e**, Field-dependent magnetization curves for the two directions measured at 2 and 300 K. **f**, Temperature- and field-dependent resistivity data. **g**, X-ray magnetic circular dichroism measurements for MnBi₂Te₄ at the Mn $L_{2,3}$ edge. A sketch of the experiment is given in the inset. The external magnetic field is applied along the direction of light incidence. The two top panels show the sum (XAS signal) and the difference (XMCD signal) between the I_R and I_L X-ray absorption intensities measured with right and left circularly polarized light in normal incidence at $\mu_0 H = 6$ T. The bottom panels show the XMCD signal in remanence, i.e. at $H = 0$ T, for normal and grazing light incidence, measured after switching off an external field of $\mu_0 H = 6$ T along the respective directions. Insets show a magnification of the L_3 dichroism in remanence.

The $M(H)$ curve acquired below T_N for $H \perp (0001)$ shows an indicative spin-flop transition at $\mu_0 H_{SF} \simeq 3.5$ T (Fig. 2e), which is in line with an out-of-plane easy axis of the staggered magnetization.

To gain additional insight into the magnetic ordering in MnBi₂Te₄, we performed X-ray magnetic circular dichroism (XMCD) experiments at the Mn $L_{2,3}$ absorption edge (Fig. 2g; D samples). The XMCD data were acquired in total electron yield (TEY) mode with a probing depth of typically only a few nm²⁹. The XMCD signal obtained at an external field of 6 T and in normal light incidence verifies a magnetic polarization of the Mn ions. After removal of the external field ($H = 0$) the XMCD signal collapses as expected for an AFM ordering. Yet, a small residual signal is still observed in remanence, indicating a finite net out-of-plane polarization within the probed volume of the sample. This residual signal appears to be

inconsistent with an AFM intralayer coupling where the orientation of the moments within a Mn layer alternates on the atomic scale. For FM intralayer coupling, however, the first SL, which is preferentially probed in the TEY mode, is expected to be composed of mesoscopic domains with the magnetization pointing in or out of the surface plane. We attribute the residual XMCD signal in remanence to a preferential sampling of one domain type with the micron-sized synchrotron beam spot. This supports our first-principles calculations predicting an FM ordering within individual SLs. Performing the same experiment in grazing light incidence, i.e. with sensitivity to in-plane magnetization, we observe no finite polarization in remanence.

Temperature- and field-dependent resistivity measurements were performed on B samples (Fig. 2f). The metallic-like behavior characteristic of the presence of

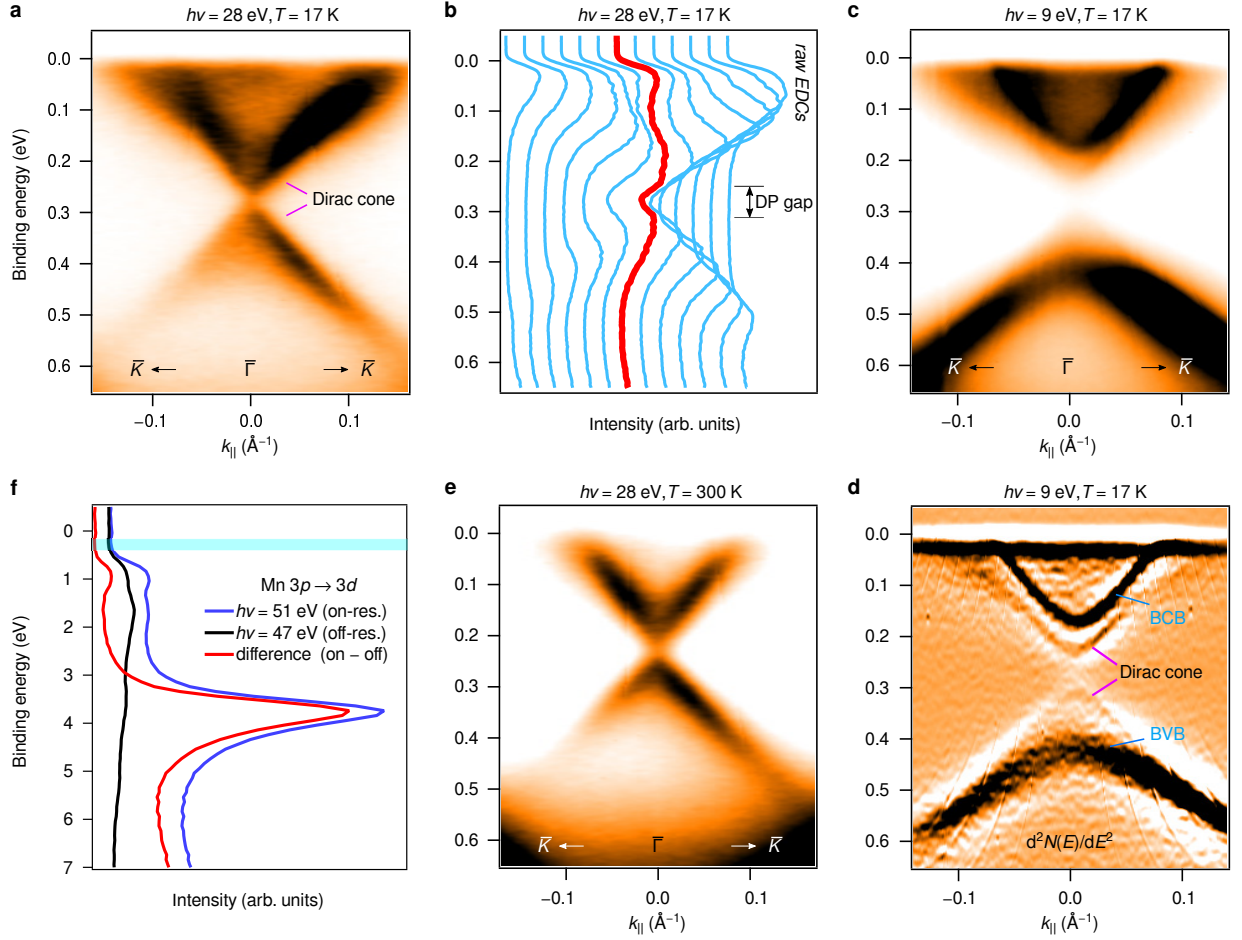


Figure 3. **a**, Dispersion of $\text{MnBi}_2\text{Te}_4(0001)$ measured at 17 K with a photon energy of 28 eV and, **b**, EDC representation of the data shown in **a**. The red curve marks the EDC at the $\bar{\Gamma}$ -point. **c**, Dispersion of $\text{MnBi}_2\text{Te}_4(0001)$ measured at the same temperature with a photon energy of 9 eV (which is more bulk sensitive) and, **d**, the corresponding second derivative, $d^2N(E)/dE^2$; BVB and BCB stand for the bulk valence and conduction bands, respectively. **e**, ARPES image acquired at 300 K ($h\nu = 28$ eV). The results shown in **a-e** were acquired on B samples. **f**, Resonant valence band spectra of MnBi_2Te_4 taken at the Mn $3p - 3d$ absorption edge (D samples). On and off-resonance spectra were obtained at $h\nu = 51$ eV and $h\nu = 47$ eV, respectively. The difference between these spectra approximately reflects the Mn $3d$ DOS showing a main peak near 3.8 eV and an additional feature near 1 eV. The energy range of the bulk energy gap is marked by cyan stripe.

free carriers, is observed at $H = 0$ as the resistivity ρ increases with rising temperature. This is consistent with the results of the Hall effect measurements revealing the n -type conductivity of these samples (Supplementary Figure 2). A well-defined kink at 25.4 K indicates a magnetic transition in agreement with the magnetization studies and Monte Carlo simulations. In a series of measurements under an external field applied normally to the (0001) plane the kink shifts to lower temperatures as the field increases from 1 T to 3 T. Above the critical field of ~ 3 T to 4 T, the $\rho(T)$ curve slope decreases much steeper below T_N , which could be related to the observed spin-flop in the $M(H)$ curve (Fig. 2e). We would like to note at this point that the $M(H)$ dependence in Fig. 2e for $H \perp (0001)$ plane shows no saturation even at a maximal field used (7 T) as the magnetization is only $\sim 3\mu_B$ per formula unit instead of $\sim 5\mu_B$. This is a clear mani-

festation of the strength of the AFM interlayer exchange coupling acting against the external magnetic field.

Altogether, the experimental scope of evidence (Fig. 2) allows to identify MnBi_2Te_4 as an interlayer antiferromagnet, in which FM Mn layers are coupled antiparallel to each other and the easy axis of staggered magnetization points perpendicular to the layers (Fig. 1d). The abovementioned statistical disorder does not affect the overall magnetic structure of MnBi_2Te_4 , which appears to be as predicted by our *ab initio* calculations and Monte Carlo simulations. Further total-energy calculations, performed for a scenario with the Mn/Bi intermixing, show that the magnetic moments of the Mn atoms at the Bi sites are coupled ferromagnetically to those in the Mn layer.

To study the surface electronic structure of $\text{MnBi}_2\text{Te}_4(0001)$ we performed angle-resolved pho-

to emission spectroscopy (ARPES) experiments. The ARPES spectrum measured near the Brillouin zone center along the $\bar{K} - \bar{\Gamma} - \bar{K}$ direction at a temperature of 17 K is shown in Fig. 3a ($h\nu = 28$ eV; B sample). One can clearly see two almost linearly dispersing bands forming a Dirac-cone-like structure with strongly reduced intensity at the crossing point. The energy distribution curves (EDCs) reveal an energy gap of about 70 meV at the $\bar{\Gamma}$ -point (Fig. 3b) that separates the upper and lower parts of the cone. A similar result was obtained for the D samples (Supplementary Figure 3). These results are in a qualitative agreement with those of the MnBi_2Te_4 surface bandstructure calculations (see Fig. 1f).

In order to identify other theoretically calculated spectral features of MnBi_2Te_4 (0001) in the ARPES maps, we performed extensive measurements at different photon energies. Careful inspection of the data acquired with $h\nu = 9$ eV (Fig. 3c) allows one to note that other features than at $h\nu = 28$ eV show a pronounced spectral weight: namely, the intense electron- and hole-like bands coming to the $\bar{\Gamma}$ -point at the binding energies of about 0.17 eV and 0.4 eV, respectively. A comparison with the theoretically calculated bulk-projected bandstructure allows to identify these bands as the bulk conduction and valence bands, respectively. The analysis of the $\bar{\Gamma}$ -point EDC shows that both valence and conduction bands can be fitted with two peaks (Supplementary Figure 4) in a qualitative agreement with the result of our calculations, showing two bulk bands with a weak k_z dispersion both below and above the Fermi level (Fig. 1f). Based on our photoemission measurements, we estimate the bulk bandgap to be close to 200 meV, again, in agreement with the calculated values. In Fig. 3d, the second derivative representation provides further insight, apart from the bulk bands revealing also the gapped Dirac cone that at $h\nu = 9$ eV appears with lower intensity.

These data confirm the $Z_2 = 1$ 3D AFMTI phase in MnBi_2Te_4 , which thus is the first experimentally identified system in the AFMTI class. To check whether the inverted character of the bulk bandgap in MnBi_2Te_4 is directly related to the AFM order we measured the surface bandstructure above T_N , at 300 K (Fig. 3e; $h\nu = 28$ eV), i.e. in the Θ -preserving paramagnetic state. It can be seen that the topological surface state does not disappear at high temperature, implying that the bulk bandgap inversion persists across the magnetic phase transition. Thus, the Θ -breaking 3D AFMTI phase in MnBi_2Te_4 is changed by the Θ -symmetric (paramagnetic) 3D TI phase above T_N . Note that increasing the temperature does not lead to the DP gap closing, which is similar to what was reported for the surface states of magnetically-doped TIs^{30–32} in the paramagnetic phase. In the case of the $\text{Bi}_{2-x}\text{Mn}_x\text{Se}_3$ (0001) surface, resonant scattering processes due to impurity in-gap states were suggested to be a possible reason of such a behavior³². To check whether similar effects take place in our MnBi_2Te_4 samples, we performed resonant photoemission measurements at the

Mn $3p - 3d$ edge. The results, shown in Fig. 3f, reveal no resonant features and, hence, no Mn- $3d$ -DOS in the region of the DP gap, whereupon we discard such a mechanism of the DP gap opening in MnBi_2Te_4 . Thus, together with previous findings^{30–33}, our results stress the importance of acquiring a better insight of how thermal paramagnetic disorder, potentially in combination with structural defects, influences the low-energy excitation spectrum near the DP in the paramagnetic phase of magnetic TIs in general. An additional solid support to the topological nontriviality of MnBi_2Te_4 comes from the results of the surface bandstructure calculations, in which the material was artificially driven into a topologically-trivial phase by suppressing the SOC constant: these results strongly disagree with those of our ARPES measurements. Namely, in the trivial phase there are neither surface states in the bulk bandgap of MnBi_2Te_4 at/near the $\bar{\Gamma}$ -point nor the resonance states near the bulk bandgap edges (Supplementary Figure 5). In contrast, our ARPES data acquired at different photon energies unambiguously confirm the gapped Dirac cone to be a surface state in agreement with the calculated surface bandstructure of the MnBi_2Te_4 AFMTI (Fig. 1f).

IV. OUTLOOK AND CONCLUSIONS

Our experimental and theoretical results establish MnBi_2Te_4 as the first observed AFMTI. Although in our experiment it is n -doped (which is typical for the bulk TI crystals), it is n -doping that allows to observe the topological surface state with ARPES, which probes only the occupied states. A common strategy in synthesizing truly insulating TI crystals is the admixture of Sb to the Bi sublattice of tetradymite-like compounds^{34–36}, which is expected to work for MnBi_2Te_4 as well. Note that such a tuning of composition is not supposed to affect its interlayer AFM ordering²³. On the other hand, recent progress in the molecular beam epitaxy growth of the TI films³⁷ rises hope that a nearly charge neutral MnBi_2Te_4 can be fabricated.

All this would constitute an important step towards many novel applications. Indeed, according to Ref. [13], an AFMTI with the type of antiferromagnetic order established here for MnBi_2Te_4 represents ideal platform for observing the half-integer quantum Hall effect ($\sigma_{xy} = e^2/(2h)$), which may aid experimental confirmation of the $\theta = \pi$ quantized magnetoelectric coupling. A material showing this effect is known as an axion insulator, which up to now was being sought for in magnetically-doped sandwich-like TI heterostructures^{38–40}. Unfortunately, the latter were found to show superparamagnetic behavior^{41–43} – a drawback that MnBi_2Te_4 does not suffer from, which makes it a promising intrinsic axion insulator candidate. Incidentally, since a possibility of realizing the $\theta \neq \pi$ dynamical axion field in the paramagnetic TI state has been pointed out recently²¹, the gap at the MnBi_2Te_4 (0001) surface above T_N might facilitate

the embodiment of this idea at room temperature. On the other hand, the FM SL blocks of MnBi_2Te_4 can be utilized for the creation of topologically-nontrivial heterostructures using the recently proposed magnetic extension effect^{33,44,45}. Unlike magnetic doping or proximity effect, it yields a giant bandgap in the topological surface state of a nonmagnetic TI thus providing a promising platform for achieving the quantum anomalous Hall effect³⁶ at elevated temperatures. Finally, beyond topotronics, another direction of further studies of MnBi_2Te_4 and related materials, such as MnBi_2Se_4 ^{23,33,46} and MnSb_2Te_4 ²³, lies within the rapidly growing field of van der Waals magnets^{47,48}. Strongly thickness-dependent properties, expected for the van der Waals compounds in the ultrathin film limit, combined with the magnetic degrees of freedom and the strong SOC present in MnBi_2Te_4 , make it an interesting candidate to couple the emerging fields of antiferromagnetic spintronics and layered van der Waals materials.

In summary, we have theoretically predicted and experimentally confirmed a three-dimensional AFMTI phase in the layered van der Waals compound MnBi_2Te_4 . These results culminate almost a decade-long search of an AFMTI material, first predicted in 2010. In a broader sense, MnBi_2Te_4 represents the first intrinsically time-reversal-breaking stoichiometric TI compound realized experimentally. As an outcome of this discovery, a number of fundamental phenomena^{9,13,14,16–18,21,36,49,50} are expected to either eventually be observed, being among them quantized magnetoelectric coupling^{13,16–18} and axion insulator state^{14,21}, or become accessible at elevated temperatures⁴⁵, like the quantum anomalous Hall effect and chiral Majorana fermions^{36,50}.

METHODS

Theoretical calculations

Electronic structure calculations were carried out within the density functional theory using the projector augmented-wave (PAW) method⁵¹ as implemented in the VASP code^{52,53}. The exchange-correlation energy was treated using the generalized gradient approximation⁵⁴. The Hamiltonian contained scalar relativistic corrections and the SOC was taken into account by the second variation method⁵⁵. In order to describe the van der Waals interactions we made use of the DFT-D2⁵⁶ and the DFT-D3^{57,58} approaches, which gave similar results. Both GGA+ U ^{59,60} and HSE06^{61–63} calculations of the bulk DOS were performed. The magnetic anisotropy energy, $E_a = E_b + E_d$, was calculated taking into account both the band contribution, $E_b = E_{\text{in-plane}} - E_{\text{out-of-plane}}$, and the energy of the classical dipole-dipole interaction.

For the equilibrium structures obtained with VASP, we calculated the Heisenberg exchange coupling constants $J_{0,j}$ also from first principles, this time using the full-potential linearized augmented plane waves (FLAPW)

formalism⁶⁴ as implemented in FLEUR⁶⁵. The GGA+ U approach was employed^{66,67}. The $J_{0,j}$ constants were extracted by Fourier inversion of the magnon energy dispersion^{65,68–70}.

The Monte Carlo (MC) simulations were based on a classical Heisenberg Hamiltonian including a magnetic anisotropy energy E_a

$$H = -\frac{1}{2} \sum_{ij} J_{ij} \hat{\mathbf{e}}_i \cdot \hat{\mathbf{e}}_j + \sum_i E_a (\hat{e}_i^z)^2, \quad (1)$$

where the magnetic moments at site i and j are described by unit vectors $\hat{\mathbf{e}}_i$ and $\hat{\mathbf{e}}_j$, respectively, and the magnetic coupling constants J_{ij} are determined by *ab initio* calculations as described above.

Crystal growth

Dresden samples (D samples)

High-quality bulk single-crystals of MnBi_2Te_4 were grown from the melt by slow cooling of a 1:1 mixture of the binaries Bi_2Te_3 and $\alpha\text{-MnTe}$. The binaries were synthesized by mechanical pre-activation and annealing of stoichiometric mixtures of the elements. Crystal size and quality could be controlled via different cooling rates within a narrow temperature region at around 600 °C and varying annealing times. Further details of crystal-growth optimization will be reported elsewhere⁷¹. Single-crystal X-ray diffraction was measured on a four-circle Kappa APEX II CCD diffractometer (Bruker) with a graphite(002)-monochromator and a CCD-detector at $T = 296(2)$ K. Mo- $K\alpha$ radiation ($\lambda = 71.073$ pm) was used. A numerical absorption correction based on an optimized crystal description⁷² was applied, and the initial structure solution was performed in JANA2006⁷³. The structure was refined in SHELXL against Fo^2 ^{74,75}. Energy dispersive X-ray spectra (EDS) were collected using an Oxford Silicon Drift X-MaxN detector at an acceleration voltage of 20 kV and a 100 s accumulation time. The EDX analysis was performed using the $P/B - ZAF$ standardless method (where Z = atomic no. correction factor, A = absorption correction factor, F = fluorescence factor, and P/B = peak to background model).

Baku samples (B samples)

The bulk ingot of the Baku sample was grown from the melt with a non-stoichiometric composition using the vertical Bridgman method. The pre-synthesized polycrystalline sample was evacuated in a conical-bottom quartz ampoule sealed under vacuum better than 10^{-4} Pa. In order to avoid the reaction of the manganese content of the sample with the silica container during the melting process, the inside wall of the ampoule was coated with graphite by thermal decomposition of acetone in an

oxygen-poor environment. The ampoule was held in the "hot" zone ($\sim 680^\circ\text{C}$) of a two-zone tube furnace of the MnBi_2Te_4 Bridgman crystal growth system for 8 h to achieve a complete homogenization of the melts. Then, it moved from the upper (hot) zone to the bottom (cold) zone with the required rate of 0.7 mm/h. Consequently, the bulk ingot with average dimensions of 3 cm in length and 0.8 cm in diameter was obtained. Further details will be reported elsewhere⁷⁶. The as-grown ingot was checked by X-ray diffraction (XRD) measurements and was found to consist of several single crystalline blocks. With the aid of XRD data high quality single crystalline pieces were isolated from different parts of the as-grown ingot for further measurements.

Magnetic measurements

The magnetic measurements as a function of temperature and magnetic field were performed on a stack of single crystals of MnBi_2Te_4 (D samples) using a SQUID (Superconducting Quantum Interference Device) VSM (Vibrating Sample Magnetometer) from Quantum Design. The temperature dependent magnetization measurements were acquired in external magnetic fields of 0.02 T and 1 T for both zero-field-cooled (zfc) and field-cooled-warming (fcw) conditions. A thorough background subtraction was performed for all the curves.

Part of the magnetic measurements were carried out in the resource center "Center for Diagnostics of Materials for Medicine, Pharmacology and Nanoelectronics" of the SPbU Science Park using a SQUID magnetometer with a helium cryostat manufactured by Quantum Design. The measurements were carried out in a pull mode in terms of temperature and magnetic field. The applied magnetic field was perpendicular to the (0001) sample surface.

ARPES measurements

The ARPES experiments were carried out at the BaDElPh beamline⁷⁷ of the Elettra synchrotron in Trieste (Italy) and BL-1 of the Hiroshima synchrotron radiation center (Japan) using p -polarization of the synchrotron radiation and laser^{78,79}. The photoemission spectra were collected on freshly cleaved surfaces. The base pressure during the experiments was better than 1×10^{-10} mbar. Part of the ARPES experiments were also carried out in the resource center "Physical methods of surface investigation" (PMSI) at the Research park of Saint Petersburg State University.

ResPES measurements

ResPES data were acquired at the HR-ARPES branch of the I05 beamline at the Diamond Light Source. The measurements were conducted at a base temperature of $T = 10$ K with a beam spot size and resolution of $A_{\text{spot}} \approx 50 \times 50 \mu\text{m}^2$ and $\Delta E \approx 20$ meV. The difference of on- and off-resonant spectra for the Mn $3p \rightarrow 3d$ transition corresponds directly to the Mn $3d$ density of states. A photon energy series was conducted in order to determine suitable transition energies. The corresponding angle integrated spectra of on-resonant ($h\nu = 51$ eV) and off-resonant ($h\nu = 47$ eV) conditions can be seen in Fig. 3f.

XMCD measurements

XMCD measurements were performed at the HECTOR end-station of the BOREAS beamline at the ALBA synchrotron radiation facility⁸⁰. The data were collected in total electron yield mode. The spot size and the resolving power of the supplied photon beam were $A_{\text{spot}} < 200 \times 200 \mu\text{m}^2$ and $E/\Delta E > 9000$, respectively. Measurements were performed at the Mn- $L_{2/3}$ edges at a temperature of 2 K, i.e. well below $T_N \simeq 24$ K.

ACKNOWLEDGMENTS

M.M.O. and E.V.C. thank A. Arnau and J.I. Cerdá for stimulating discussions. We acknowledge the support by the Basque Departamento de Educacion, UPV/EHU (Grant No. IT-756-13), Spanish Ministerio de Economia y Competitividad (MINECO Grant No. FIS2016-75862-P), and Tomsk State University competitiveness improvement programme (project No. 8.1.01.2017). The supports by the Saint Petersburg State University grant for scientific investigations (Grant No. 15.61.202.2015), Russian Science Foundation (Grant No. 18-02-00062), and the Science Development Foundation under the President of the Republic of Azerbaijan (Grant No. EIF-BGM-4-RFTF-1/2017-21/04/1-M-02) are also acknowledged. A.U.B.W., A.I., and B.B. acknowledge support by the DFG within the SFB 1143. A.Z., A.E., and A.I. acknowledge the support by the German Research Foundation (DFG) in the framework of the Special Priority Program (SPP 1666) Topological Insulators and by the ERA-Chemistry Program. S.V.E. acknowledges support by the Fundamental Research Program of the State Academies of Sciences for 2013–2020. A.K. was financially supported by KAKENHI number 17H06138 and 18H03683. The calculations were performed in Donostia International Physics Center, in the Research park of St. Petersburg State University Computing Center (<http://cc.spbu.ru>), and in Tomsk State University.

- * mikhail.otrokov@gmail.com
- ¹ E. V. Gomonay and V. M. Loktev, *Low Temp. Phys.* **40**, 17 (2014),
 - ² T. Jungwirth, X. Marti, P. Wadley, and J. Wunderlich, *Nat. Nanotech.* **11**, 231 (2016).
 - ³ V. Baltz, A. Manchon, M. Tsoi, T. Moriyama, T. Ono, and Y. Tserkovnyak, *Rev. Mod. Phys.* **90**, 015005 (2018),
 - ⁴ T. Jungwirth, J. Sinova, A. Manchon, X. Marti, J. Wunderlich, and C. Felser, *Nat. Phys.* **14**, 200 (2018).
 - ⁵ R. Duine, K.-J. Lee, S. S. Parkin, and M. D. Stiles, *Nat. Phys.* **14**, 217 (2018).
 - ⁶ O. Gomonay, V. Baltz, A. Brataas, and Y. Tserkovnyak, *Nat. Phys.* **14**, 213 (2018).
 - ⁷ J. Železný, P. Wadley, K. Olejník, A. Hoffmann, and H. Ohno, *Nat. Phys.* **14**, 220 (2018).
 - ⁸ P. Němec, M. Fiebig, T. Kampfrath, and A. Kimel, *Nat. Phys.* **14**, 229 (2018).
 - ⁹ L. Šmejkal, Y. Mokrousov, B. Yan, and A. H. MacDonald, *Nat. Phys.* **14**, 242 (2018).
 - ¹⁰ M. Z. Hasan and C. L. Kane, *Rev. Mod. Phys.* **82**, 3045 (2010).
 - ¹¹ X.-L. Qi and S.-C. Zhang, *Rev. Mod. Phys.* **83**, 1057 (2011).
 - ¹² A. Bansil, H. Lin, and T. Das, *Rev. Mod. Phys.* **88**, 021004 (2016),
 - ¹³ R. S. K. Mong, A. M. Essin, and J. E. Moore, *Phys. Rev. B* **81**, 245209 (2010),
 - ¹⁴ R. Li, J. Wang, X.-L. Qi, and S.-C. Zhang, *Nat. Phys.* **6**, 284 (2010).
 - ¹⁵ S. Ghosh and A. Manchon, *Phys. Rev. B* **95**, 035422 (2017),
 - ¹⁶ X.-L. Qi, T. L. Hughes, and S.-C. Zhang, *Phys. Rev. B* **78**, 195424 (2008),
 - ¹⁷ A. M. Essin, J. E. Moore, and D. Vanderbilt, *Phys. Rev. Lett.* **102**, 146805 (2009),
 - ¹⁸ W.-K. Tse and A. H. MacDonald, *Phys. Rev. Lett.* **105**, 057401 (2010),
 - ¹⁹ H. Ooguri and M. Oshikawa, *Phys. Rev. Lett.* **108**, 161803 (2012),
 - ²⁰ A. Sekine and K. Nomura, *J. Phys. Soc. Jpn.* **83**, 104709 (2014), <https://doi.org/10.7566/JPSJ.83.104709>,
 - ²¹ J. Wang, B. Lian, and S.-C. Zhang, *Phys. Rev. B* **93**, 045115 (2016),
 - ²² D. S. Lee, T.-H. Kim, C.-H. Park, C.-Y. Chung, Y. S. Lim, W.-S. Seo, and H.-H. Park, *CrystEngComm* **15**, 5532 (2013),
 - ²³ S. V. Eremeev, M. M. Otrokov, and E. V. Chulkov, *J. Alloys Compd.* **709**, 172 (2017).
 - ²⁴ C. Fang, M. J. Gilbert, and B. A. Bernevig, *Phys. Rev. B* **88**, 085406 (2013),
 - ²⁵ S. Chadov, X. Qi, J. Kübler, G. H. Fecher, C. Felser, and S. C. Zhang, *Nat. Mater.* **9**, 541 (2010).
 - ²⁶ H. Lin, L. A. Wray, Y. Xia, S. Xu, S. Jia, R. J. Cava, A. Bansil, and M. Z. Hasan, *Nat. Mater.* **9**, 546 (2010).
 - ²⁷ O. Karpinskii, L. Shelimova, and M. Kretova, *Inorg. Mater.* **33**, 793 (1997).
 - ²⁸ K. Okamoto, K. Kuroda, H. Miyahara, K. Miyamoto, T. Okuda, Z. S. Aliev, M. B. Babanly, I. R. Amiraslanov, K. Shimada, H. Namatame, et al., *Phys. Rev. B* **86**, 195304 (2012),
 - ²⁹ M. Abbate, J. B. Goedkoop, F. M. F. d. Groot, M. Grioni, J. C. Fuggle, S. Hofmann, H. Petersen, and M. Sacchi, *Surf. Interface Anal.* **18**, 65 (1992).
 - ³⁰ Y. L. Chen, J. H. Chu, J. G. Analytis, Z. K. Liu, K. Igarashi, H. H. Kuo, X. L. Qi, S. K. Mo, R. G. Moore, D. H. Lu, et al., *Science* **329**, 659 (2010).
 - ³¹ S.-Y. Xu, M. Neupane, C. Liu, D. Zhang, A. Richardella, L. A. Wray, N. Alidoust, M. Leandersson, T. Balasubramanian, J. Sanchez-Barriga, et al., *Nat. Phys.* **8**, 616 (2012).
 - ³² J. Sánchez-Barriga, A. Varykhalov, G. Springholz, H. Steiner, R. Kirchschlager, G. Bauer, O. Caha, E. Schierle, E. Weschke, A. Ünal, et al., *Nat. Commun.* **7**, 10559 (2016).
 - ³³ T. Hirahara, S. V. Eremeev, T. Shirasawa, Y. Okuyama, T. Kubo, R. Nakanishi, R. Akiyama, A. Takayama, T. Hagiiri, S. Ideta, et al., *Nano Lett.* **17**, 3493 (2017).
 - ³⁴ J. Zhang, C.-Z. Chang, Z. Zhang, and et al., *Nat. Commun.* **2**, 574 (2011).
 - ³⁵ T. Arakane, T. Sato, S. Souma, and et al., *Nat. Commun.* **3**, 636 (2012).
 - ³⁶ C.-Z. Chang, J. Zhang, X. Feng, J. Shen, Z. Zhang, M. Guo, K. Li, Y. Ou, P. Wei, L.-L. Wang, et al., *Science* **340**, 167 (2013).
 - ³⁷ L. Wu, M. Salehi, N. Koirala, J. Moon, S. Oh, and N. P. Armitage, *Science* **354**, 1124 (2016).
 - ³⁸ M. Mogi, M. Kawamura, R. Yoshimi, A. Tsukazaki, Y. Kozuka, N. Shirakawa, K. Takahashi, M. Kawasaki, and Y. Tokura, *Nat. Mater.* **16**, 516 (2017).
 - ³⁹ M. Mogi, M. Kawamura, A. Tsukazaki, R. Yoshimi, K. S. Takahashi, M. Kawasaki, and Y. Tokura, *Sci. Adv.* **3**, eaal669 (2017).
 - ⁴⁰ D. Xiao, J. Jiang, J.-H. Shin, W. Wang, F. Wang, Y.-F. Zhao, C. Liu, W. Wu, M. H. W. Chan, N. Samarth, et al., *Phys. Rev. Lett.* **120**, 056801 (2018),
 - ⁴¹ E. O. Lachman, A. F. Young, A. Richardella, J. Cuppens, H. Naren, Y. Anahory, A. Y. Meltzer, A. Kandala, S. Kempinger, Y. Myasoedov, et al., *Sci. Adv.* **1**, e1500740 (2015).
 - ⁴² E. O. Lachman, M. Mogi, J. Sarkar, A. Uri, K. Bagani, Y. Anahory, Y. Myasoedov, M. E. Huber, A. Tsukazaki, M. Kawasaki, et al., *npj Quantum Mater.* **2**, 70 (2017).
 - ⁴³ J. A. Krieger, C.-Z. Chang, M.-A. Hsuanu, D. Sostina, A. Ernst, M. M. Otrokov, T. Prokscha, T. Schmitt, A. Suter, M. G. Vergniory, et al., *Phys. Rev. B* **96**, 184402 (2017),
 - ⁴⁴ M. M. Otrokov, T. V. Menshchikova, I. P. Rusinov, M. G. Vergniory, V. M. Kuznetsov, and E. V. Chulkov, *JETP Lett.* **105**, 297 (2017).
 - ⁴⁵ M. M. Otrokov, T. V. Menshchikova, M. G. Vergniory, I. P. Rusinov, A. Y. Vyazovskaya, Y. M. Koroteev, G. Bihlmayer, A. Ernst, P. M. Echenique, A. Arnau, et al., *2D Mater.* **4**, 025082 (2017).
 - ⁴⁶ J. A. Hagmann, X. Li, S. Chowdhury, S.-N. Dong, S. Rouvimov, S. J. Pookpanratana, K. M. Yu, T. A. Orlova, T. B. Bolin, C. U. Segre, et al., *New J. Phys.* **19**, 085002 (2017),
 - ⁴⁷ C. Gong, L. Li, Z. Li, H. Ji, A. Stern, Y. Xia, T. Cao, W. Bao, C. Wang, Y. Wang, et al., *Nature* **546**, 265 (2017).
 - ⁴⁸ B. Huang, G. Clark, E. Navarro-Moratalla, D. R. Klein, R. Cheng, K. L. Seyler, D. Zhong, E. Schmidgall, M. A. McGuire, D. H. Cobden, et al., *Nature* **546**, 270 (2017).

- ⁴⁹ A. Sekine and K. Nomura, Phys. Rev. Lett. **116**, 096401 (2016),
- ⁵⁰ Q. L. He, L. Pan, A. L. Stern, E. C. Burks, X. Che, G. Yin, J. Wang, B. Lian, Q. Zhou, E. S. Choi, et al., Science **357**, 294 (2017).
- ⁵¹ P. E. Blöchl, Phys. Rev. B **50**, 17953 (1994).
- ⁵² G. Kresse and J. Furthmüller, Phys. Rev. B **54**, 11169 (1996).
- ⁵³ G. Kresse and D. Joubert, Phys. Rev. B **59**, 1758 (1999).
- ⁵⁴ J. P. Perdew, K. Burke, and M. Ernzerhof, Phys. Rev. Lett. **77**, 3865 (1996).
- ⁵⁵ D. D. Koelling and B. N. Harmon, J. Phys. C: Sol. St. Phys. **10**, 3107 (1977).
- ⁵⁶ S. Grimme, J. Comput. Chem. **27**, 1787 (2006).
- ⁵⁷ S. Grimme, J. Antony, S. Ehrlich, and H. Krieg, J. Chem. Phys. **132**, 154104 (2010).
- ⁵⁸ S. Grimme, S. Ehrlich, and L. Goerigk, J. Comput. Chem. **32**, 1456 (2011).
- ⁵⁹ V. I. Anisimov, J. Zaanen, and O. K. Andersen, Phys. Rev. B **44**, 943 (1991).
- ⁶⁰ S. L. Dudarev, G. A. Botton, S. Y. Savrasov, C. J. Humphreys, and A. P. Sutton, Phys. Rev. B **57**, 1505 (1998).
- ⁶¹ A. D. Becke, Phys. Rev. A **38**, 3098 (1988).
- ⁶² J. P. Perdew, M. Ernzerhof, and K. Burke, J. Chem. Phys. **105**, 9982 (1996).
- ⁶³ J. Heyd, G. E. Scuseria, and M. Ernzerhof, J. Chem. Phys. **118**, 8207 (2003).
- ⁶⁴ E. Wimmer, H. Krakauer, M. Weinert, and A. J. Freeman, Phys. Rev. B **24**, 864 (1981),
- ⁶⁵ FLEUR site: <http://www.flapw.de>.
- ⁶⁶ V. I. Anisimov, F. Aryasetiawan, and A. I. Lichtenstein, Journal of Physics: Condensed Matter **9**, 767 (1997),
- ⁶⁷ A. B. Shick, A. I. Lichtenstein, and W. E. Pickett, Phys. Rev. B **60**, 10763 (1999),
- ⁶⁸ L. M. Sandratskii and P. Bruno, Phys. Rev. B **66**, 134435 (2002),
- ⁶⁹ M. Ležaić, P. Mavropoulos, J. Enkovaara, G. Bihlmayer, and S. Blügel, Phys. Rev. Lett. **97**, 026404 (2006),
- ⁷⁰ P. Kurz, F. Förster, L. Nordström, G. Bihlmayer, and S. Blügel, Phys. Rev. B **69**, 024415 (2004),
- ⁷¹ A. Zeugner et al., In preparation (2018).
- ⁷² X-Shape, Crystal Optimization for Numerical Absorption Correction Program. v. 2.12.2, Stoe & Cie GmbH, Darmstadt, 2009.
- ⁷³ V. Petricek, M. Dusek, and L. Palatinus, *JANA2006, The Crystallographic Computing System* (Institute of Physics, Praha, Czech Republic, 2011).
- ⁷⁴ G. M. Sheldrick, *SHELXL, Program for Crystal Structure Refinement Multi-CPU v. 2014/7* (Georg-August-Universität Göttingen, Göttingen, Germany, 2014).
- ⁷⁵ G. M. Sheldrick, Acta Cryst. A **64**, 112 (2008).
- ⁷⁶ Z. S. Aliev et al., In preparation (2018).
- ⁷⁷ L. Petaccia, P. Vilmercati, S. Gorovikov, M. Barnaba, A. Bianco, D. Cocco, C. Masciovecchio, and A. Goldoni, Nucl. Instrum. Methods Phys. Res. A **606**, 780 (2010).
- ⁷⁸ H. Iwasawa, K. Shimada, E. F. Schwier, M. Zheng, Y. Kojima, H. Hayashi, J. Jiang, M. Higashiguchi, Y. Aiura, H. Namatame, et al., J. Synchrotron Rad. **24**, 836 (2017),
- ⁷⁹ H. Iwasawa, E. F. Schwier, M. Arita, A. Ino, H. Namatame, M. Taniguchi, Y. Aiura, and K. Shimada, Ultramicroscopy **182**, 85 (2017).
- ⁸⁰ A. Barla, J. Nicolás, D. Cocco, S. M. Valvidares, J. Herrero-Martín, P. Gargiani, J. Moldes, C. Ruget, E. Pellegrin, and S. Ferrer, J. Synchrotron Rad. **23**, 1507 (2016).